MERCURY: A NOVEL DESIGN FOR A BACK JUNCTION BACK CONTACT CELL WITH FRONT FLOATING EMITTER FOR HIGH EFFICIENCY AND SIMPLIFIED PROCESSING

I. Cesar, N. Guillevin, A.R. Burgers, A.A. Mewe, E.E. Bende, V. Rosca, B. van Aken, M. Koppes, J. Anker, L.J. Geerligs, A.W. Weeber ECN Solar Energy, P.O. Box 1, 1755 ZG Petten, The Netherlands, cesar@ecn.nl

ABSTRACT: The back junction back contact cell, and more specifically the interdigitated back contact (IBC) cell is among the most appropriate cell design to achieve high cell efficiency. An important aspect to improve manufacturability (e.g. reduce cost) of the cell and module is allowing larger feature sizes for the different regions at the rear, for example the BSF. We propose a novel design of an IBC cell that enhances the effective lateral transport of minority carriers (holes) and therefore allowing wide BSF regions. The novel design features an appropriate conductive and well passivated p++-doped layer, referred to as a front floating emitter (FFE), on the front surface of the IBC cell. This conductive FFE enables equally-sized interdigitated doping patterns of positive and negative polarities on the rear, with similar cell pitch and efficiency compared to traditional IBC cells. It also enables larger interconnection pads for easier module interconnection with marginal performance loss. Additional advantages are expected such as relaxed alignment tolerances for patterning as well as interconnection processes. We report on the proof-of-principle of this new cell concept, which we name "Mercury", brought forward by 2D simulations and experimental results on small and 6 inch cells. So far, based on an industrial process flow with stable results, these cells yield full area efficiencies up to 19.6% on 6 inch and short-circuit densities well above 41 mA/cm² for masked smaller cells. Additionally, the Mercury cells show comparable efficiency loss at low illumination intensity as to standard p-type H-pattern cell. Furthermore, we present the interconnection and cell design of our 6 inch Mercury cell and prove that our first 4-cell Mercury modules pass the thermal cycling and damp heat test equivalent to the IEC protocol demands.

Keywords: Front floating emitter, IBC, n-type silicon, solar cell, electrical shading, back surface field, module

1 INTRODUCTION

IBC cell technology is ideal for high-efficiency solar cells mainly because all metallization can be applied to the rear side of the cell which eliminate shading losses. The industrial manufacturability of these cells has been demonstrated by Sunpower for many years. Recently, the company reported on the industrial production of 5 inch IBC cells with median efficiencies as high as 25% [1]. Recent achievements by others are worth mentioning. A consortium of ANU and Trina have reported on a 2x2 cm² IBC cell with a top efficiency of 24.6% featuring local back surface field (BSF) diffusions at the contacts and an non-diffused front side that is passivated by a dielectric stack [2]. IMEC obtained on 2x2 cm² 23.1% [3]. A process based on implanted surface diffusions is reported by Bosch Solar achieving 22.1% on 239 cm² cells [4]. Also, Samsung together with Varian reported on IBC cells prepared by implantation on 155 cm² with 22.4% efficiency [5]. The high performance of these cells is partially obtained by means of contact technologies such as PVD in combination with electroplating. These contacts exhibit much lower contact recombination losses than the conventional screen-print technology based on fire-through silver pastes. However, ISC Konstanz has reported on 6 inch IBC cells with screen-printed contacts with up to 21.3% efficiency, illustrating the potential of that low-cost approach [6]. Also Hareon presented on screen printed IBC solar cell and achieved 19.6% in 6 inch Cz [7]. Earlier this year ECN has reported on 6 inch IBC cells with industrial processing and screen-printed contacts with an efficiency up to 19.0% [8]. Recently, Müller et al. reported on an attractive process flow for an FFE IBC cell that reached 21.7% on 2x2 cm based on Pimplantation that selectively blocked the following BBr₃ diffusion [9].

Although interdigitated back contact (IBC) solar cells have shown to yield very high conversion efficiencies, cost effective production of these devices poses challenges. To allow all contacts to be applied to the rear of the cell, the rear collecting junction (the emitter) is interrupted by a non-collecting junction (the BSF) as illustrated in figure 1. Therefore, any carrier that is photogenerated above a BSF area needs to travel laterally to an emitter area. If the BSF regions become too wide, the collection probability of carriers generated above the BSF will decrease: an effect referred to as electrical shading [10]. To prevent loss in cell performance, the typical width of the BSF is in the order of 0.2-0.4 mm out of a typical cell pitch of 1.5 mm.

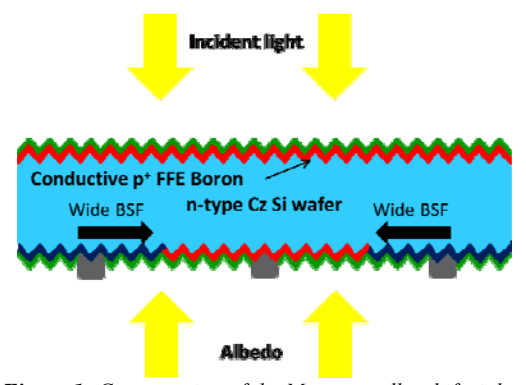


Figure 1: Cross-section of the Mercury cell; a bifacial n-IBC solar cell with screen-printed contacts.

The inequality of BSF and emitter widths results in strict patterning tolerances for processing but has also implications for the metallization as shown in our previous report [8]. Equal widths of both polarities allow

to metallize the IBC cell with blanket metallization technologies such as PVD and plating without the need of an isolation layer. This is a significant process simplification and opportunity for cost reduction.

In this paper we report on a novel design variation of the traditional IBC cell, meant to enhance lateral transport properties for minority carriers. Owing to the enhanced transport distance, it simply allows the BSF width to be as wide as the emitter width without significant loss in cell efficiency. This enhancement is achieved by implementing a p⁺-doped layer on the frontside of the n-type IBC Mercury cell. This p⁺-doped layer, also referred to as front floating emitter (FFE), induces a pumping effect on the minority carriers in the base (holes) and redirect them from regions above the BSF to the rear emitter as illustrated in Figure 2 (discussed in more detail in section 2). Although front floating emitters have been investigated in the past [9, 11-20], the novelty presented in this paper resides in the proper tuning of the conductivity of the FFE and of the wafer in combination with cell structure dimensions. With proper tuning, the FFE can be applied as an effective means to increase the BSF width with marginal loss in cell performance while assuring process simplification and cost reduction. Besides this, the new design leads to more freedom in the interconnection lay-out and increases the tolerances for the module fabrication. We name this invention the Mercury cell, in reference to the planets' proximity to the sun. We present both 2D numerical simulation results and experimental evidence for the working principle. Moreover, we present the cell and interconnection design of the 6 inch Mercury cell as well as the first reliability results of 4-cell IBC modules based on a conductive back-sheet foil that was previously developed for our MWT module technology [21-23].

2 BENEFIT OF A CONDUCTIVE FRONT FLOATING EMITTER

2.1 Working principle of the Mercury cell

The working principle of an IBC cell with a front floating emitter has been explained in previous work in terms of equivalent circuits that prominently incorporate a transistor element to describe the p/n/p bipolar transistor action above the rear emitter [15-16]. Here we focus on the relation between electrical shading and cell design parameters such as the resistance of the FFE, the resistance of the wafer and the BSF width.

To illustrate the benefit of the FFE vs. the FSF, the concentration and vector plots of holes are drawn in cross-sections of a unit cell for both cell types, as shown in Figure 2. The case simulated with Atlas, a 2D simulation software package (see section 2.3 for simulation details), investigates a unit cell with an extremely wide BSF of 1.2 mm (0.6 mm from BSF centre to nearest emitter edge) which leads to large electrical shading losses for conventional IBC cells with an FSF or non-diffused front surfaces.

In an FSF cell under illumination, holes generated above the BSF diffuse to the emitter in the direction parallel to the surface as shown in Figure 2b. As the path length to the emitter contact is large compared to the diffusivity and lifetime of holes, the concentration in the bulk increases creating a concentration gradient that drives the hole current density towards the hole collection region (emitter). This narrow region near the BSF / Emitter

junction collects holes with a relatively large current density as illustrated by the red vector arrows in Figure 2b.

In the case of the Mercury type cell however, the lateral hole transport mechanism relies mainly on the conductive path provided by the front floating emitter. The working principle of the Mercury cell can be explained by an asymmetry in the working point of the I-V curves of the FFE-base junction. The FFE collects holes from the base as illustrated in the hole vector plot in Figure 2d. Since the FFE is not contacted (floating), these carriers are not extracted and the FFE-base junction will be charged towards open circuit condition. If the FFE is conductive enough the voltage is constant at the full surface of the wafer. Above the emitter, both the FFE and the rear emitter junction can collect carriers. Above the BSF however, hole collection is not divided between a front and rear junction and thus the FFE – base junction collects most of the holes. Hence, the photocurrent across the FFE-base junction is larger above the BSF than above the rear emitter. Consequently, the open circuit voltage of the FFE-base junction is higher above the BSF than above the rear emitter. Because the FFE-base junction above the BSF is floating, there will be no net current flowing in or out of the FFE. Because of the laterally constant potential in the FFE, the FFE will achieve a voltage at which the collection of carriers from above the BSF will match the injection of carriers from the FFE into the base above the rear emitter. This sets up a hole transport "conveyor belt" also referred to the "pumping effect": minorities (holes) generated above the BSF are collected in the FFE and transported as majorities towards regions above the rear emitter, where they are re-injected into the base and subsequently collected by the rear emitter. Effectively, the front junction collects the minority carriers from the base above the BSF region and transports them to the section where the front emitter overlaps with the emitter on the rear, as is presented in in Figure 2. A more elaborate illustration of the effects mentioned here are discussed in a previous

This current flow from FFE to emitter will occur in parallel to the diffusion of minority carriers directly from the base to the rear emitter junction. In addition to providing enhanced lateral transport, the pumping effect drastically reduces carrier levels in the base above the BSF at short-circuit conditions, and hence the recombination rate in the base as illustrated in Figure 2a and 2c: the minority carrier densities is a factor 10 higher in the base of an FSF cell than in the base of an FFE cell.

The re-injection of carriers from the FFE above the emitter into the base leads however to a higher hole concentration near the front surface above the rear emitter junction compared to the FSF case, as can be seen in Figure 2 a and c. However, much smaller hole concentration gradients are required for vertical transport (from FFE to rear emitter) than for horizontal transport (from rear BSF to the rear emitter). This is explained by the geometry of the system. For the vertical transport from the FFE to the rear emitter, the full emitter width (0.8 µm half-width in the unit cell) is available, whereas for the horizontal hole transport in the FSF case, only the wafer thickness is available (145 µm). So the same concentration gradient can transport more carriers in the FFE case. In addition, the vertical transport distance from the FFE to the emitter is much smaller than across the BSF width to the emitter, leading to lower carrier concentrations, and therefore less recombination. The pumping effect of the FFE cell hence allows to increase the pitch of the cell, while maintaining a good current.

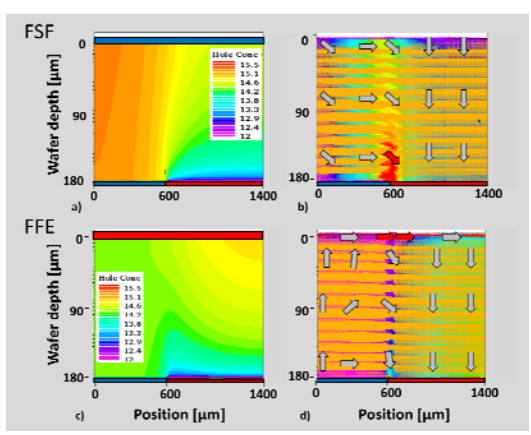


Figure 2:: Simulated (Atlas) performance comparison ($R_{bulk} = 9 \ \Omega$ -cm, $\tau_{bulk} = 2.5 \ ms$, $R_{sht,FFE} = 65 \ \Omega/\Box$, $R_{sht,FSF} = 140 \ \Omega/\Box$) of the n-IBC cell with FSF or FFE on n-type wafer at J_{sc} condition. Image a & c) are illustrations of the hole carrier density of an extremely wide BSF of 1.2 mm (full width). Images b) and d) are vector plots illustrating the size and direction of the holes current for an FSF cell (b) and FFE cell (d). The y-axis measures the distance from the top surface into the wafer in μ m and the x-axis measures the distance from the centre of the BSF (blue bar) to the centre of the emitter (red bar). The image is not drawn to scale. The red arrows in the vector plots indicate high current densities.

2.2 Simulated LBIC of Mercury cell

The working principle of the Mercury cell relies on the hole transport through the FFE. If the FFE is too resistive, this hole transport would not be possible, and one would expect electrical shading. In addition to the conductivity in the FFE, the sheet resistance of the base of the cell is an important parameters that influences the transport through the FFE as discussed in our previous publication [8].

In order to illustrate these effects, simulations of LBIC (Light Beam Induced Current) measurements were performed with the Atlas software. The simulation was done for both FSF and FFE configurations. In both cases we considered FFE and FSF sheet resistances of 70 Ω/\Box and $1000~\Omega/\Box$. The cell configuration and models are the same as used for Figure 2, exhibiting significant electrical shading losses for the standard FSF IBC cell, with a 1.2 mm wide BSF and a 1.6 mm wide emitter.

The bias light spectrum was AM1.5, the LBIC light was a 50 μ m wide beam, monochromatic, 970 nm wavelength, with an intensity within the beam of 10 mW/cm². For a unit cell width of 1.4 mm and this wavelength the beam can contribute 0.28 mA/cm² to the cell current.

Such an LBIC simulation is quite different from a practical LBIC measurement, as it consists of a 2-D device simulation on a cross-section. Therefore, the LBIC "spot" becomes a line source. Moreover the line source is applied on a unit cell. In an actual LBIC measurement only one unit cell would typically be illuminated with the LBIC spot, while here all unit cells are illuminated.

Figure 3 presents the hole density plots discussed in the previous section over a device width of 4 unit cells and the results of the LBIC simulations, expressed as IQE. For 2 and 9 Ω -cm bulk resistivity, the wafer has a sheet resistance of 138 and 621 Ω / \Box respectively.

In the FSF cell case, the lower LBIC signal above the wide BSF is typical for electrical shading losses. Also, the FSF conductivity does hardly affect the LBIC response, although it has an effect on the FF: a more conductive FSF leads to a better FF. The poor local IQE in the case of the FSF cell overlaps with the BSF region with high hole densities which results in higher SRH and Auger recombination and thus lower IQE.

The LBIC curves for the FFE case are quite different. The conductive FFE helps in maintaining a high IQE over the BSF region (n^{++}) especially in the case of a conductive wafer (2 Ω -cm), thus mitigating the electrical shading losses. A too high FFE sheet resistance weakens this mitigating effect to a large extent. As mentioned before, compared to the FSF cell, the hole densities above the BSF are 10 times lower in the FFE cell due to the pumping effect. This is the main cause for the high IQE over the full width of the illustrated device.

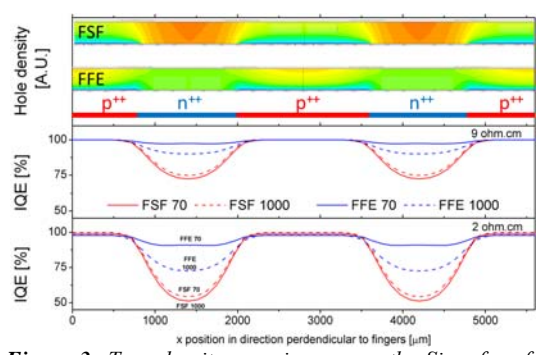


Figure 3: Top: density mapping across the Si wafer of Figure 2 drawn to scale showing the FSF and the FFE IBC solar cell. The front diffusions have a Rsheet of 70 Ω / \square and base thickness and reistance of 145 μ m and 9 Ω -cm respectively. The 1.2 mm wide BSF (n++) and the 1.6 mm wide rear emitter (p+) region are marked in the collored bar. Bottom: the local IQE mapping across several unit cells with FSF and FFE front diffusions with Rwafer of 2 and 9 Ω -cm and R_{sheet} front diffusion values of 70 and 1000 Ω / \square .

For the Mercury cell the base resistivity plays an important role. The lateral transport of majority carriers (electrons) above the emitter towards the BSF, induces a voltage gradient above the emitter. This gradient promotes the pumping effect. This is also the reason why the pumping effect depends strongly on the base resistance, especially in case of a more resistive FFE. It is less effective for lower resistivity material or thicker wafers

Commercial n-type material available to the PV market consists of a broad range of wafer resistivities inherent to the ingot growth process. From the results above we can conclude that to achieve good J_{sc} values for cells with wide BSF regions across such a resistivity range (i.e. across a ingot), one best applies a conductive FFE as is proposed in the Mercury cell. This means that highly performing cells can be fabricated from a large part of the silicon ingot.

2.3 Cell design and performance

The contour plots shown in Figure 4 result from 2D simulations conducted with the Quokka software [24],

and demonstrate that the lateral effective transport length can be increased and that the electrical shading losses as well as cell efficiency are less dependent on the BSF width in the Mercury concept than in the conventional IBC cell with FSF. Thus, comparable efficiencies can be reached using increased design tolerances which translates into ease of manufacturing.

Also in this simulation, the most striking difference between both cell types is the J_{sc} behaviour for changing width of emitter and BSF. Whereas the J_{sc} plummets for the FSF cell with broad BSF widths due to electrical shading losses, the FFE cell maintains high currents for a large part of the parameter space. The fill factor of the FFE cell is slightly lower than of the FSF cell while the Voc is identical as the Jo values are kept similar for both cells (both not shown here). The FF calculations presented in Figure 4, exclude ohmic losses in the contacts, fingers and busbars. The resulting efficiency plots clearly show that high cell efficiencies can be obtained for a broad range of cell geometries including the case of equal emitter and BSF widths and reasonable cell pitch which are preferred with respect to the optimal metallization solutions as discussed earlier [8].

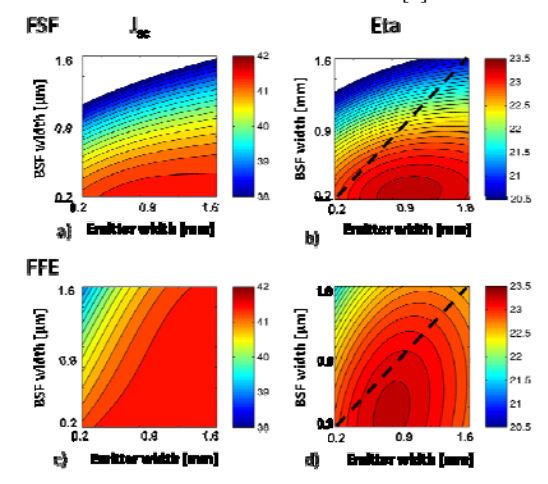


Figure 4: Modelled performance comparison of the IBC cell with FSF and FFE. The IV parameters J_{sc} and cell efficiency are presented as a function of emitter and BSF width. The values shown are full widths, expressed in mm. The diagonal dashed line in b) and d) indicates cell designs with equal widths for emitter and BSF. The input parameter are tabulated in the appendix.

To illustrate the potential of the Mercury cell, with conductive FFE and broad BSF, we evaluated the conversion efficiency dependency on the cell emitter and BSF widths. We compare three cases as function of BSF widths: 1) the optimal efficiency of FSF IBC, 2) the optimal case of the FFE IBC cell and 3) the FFE cell with the constraint that the width of the BSF is equal to the emitter width.

The peak efficiencies for narrow BSF width are very close at 23.5% for both the FSF and FFE. As the BSF width increases, the peak efficiency for the FSF case quickly decreases. The FFE case also shows a decrease but much more slowly. The efficiency for the FFE (wBSF=wemitter case) is clearly lower for narrow BSFs. However, at a 1.0 mm full width for BSF and emitter, an efficiency of 23.2% can still be reached with a $V_{\rm oc}$ of 688 mV, a $J_{\rm sc}$ of 41.4mA/cm2 and a FF of 81.3%.

To illustrate the dependency on the Rsheet of the FFE also the case with $200~\Omega/\Box$ is illustrated which shows that for a 1.0 mm wide BSF only 0.1% abs is lost compared to the more conductive FFE. This shows that the conductivity is this range is rather forgiving and that the targeted J_o of FFE of 15 fA/cm² is more likely to be experimentally achieved with this lighter diffusion.

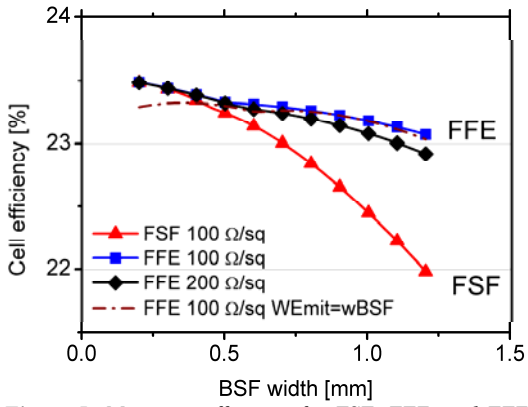


Figure 5: Maximum efficiency for FSF, FFE, and FFE IBC (with the constraint wBSF=wemitter) for a given BSF width. In Figure 4 one can look up for each BSF width 1) the maximum $100~\Omega/\Box$ FSF η , 2) the maximum $100~\Omega/\Box$ FFE η , 3) the maximum $100~\Omega/\Box$ FFE η (with the constraint wBSF=wemitter, dashed lines in the contour plot). The maximum eta for $200~\Omega/\Box$ is also added but no contour plots are shown.

It should be noted that at lower bulk lifetimes the electrical shading losses in the FSF cell increase more strongly than for the FFE cell due to the lower carrier density in the Mercury cell as discussed above. Consequently, the benefits of the Mercury cell are more pronounced at bulk lifetimes lower than the 4 ms as used in the illustrated simulation.

2.3 Experimental validation

Wafers with different bulk resistivity (2, 4, 7 and 9 $\Omega\text{-cm})$ were taken from a single ingot to study the effect of the wafer resistivity and BSF width on the I-V parameters of the Mercury cell. Mercury cells featuring an emitter width of 1.6 mm and three different BSF widths (0.6, 1.2 and 1.6 mm) were manufactured. The clear J_{sc} trends are presented in Figure 6. In all cases, the J_{sc} increases with higher wafer resistivity (ρ) in accordance to the LBIC results discussed in section 2.2. In addition, the slope of the J_{sc} as function of the BSF width decreases with ρ . Generally, for both IBC cells, but mostly for the FSF IBC cell, J_{sc} suffers from higher

doping levels due to higher SRH and Auger recombination in the BSF. However, the pumping effect for the FFE cell is also enhanced by the higher wafer resistance as discussed in section 2. Consequently, J_{sc} is nearly independent on the BSF width for the cells with high ρ wafers, whereas J_{sc} significantly decreases when BSF width increases for low ρ wafers.

The experimental results are compared to simulations conducted in Atlas (Silvaco) as illustrated in Figure 6. It can be seen that the simulated results follow the experimental results quite well. For that purpose, a crosssection perpendicular to the fingers was simulated. The unit cell consists of half of a BSF width and half of an emitter width. The physical models used were Klaassen's Unified Low-Field Mobility model, a Saturation Velocity Model according to Caughey and Thomas, Fermi-Dirac statistics, Klaassen's bandgap narrowing model, radiative recombination, temperature and concentration dependent Auger recombination and SRH recombination. Surfaces were treated as flat, however the increased recombination activity due to surface area increase by presence of a pyramidal texture was taken into account by multiplying Auger recombination coefficients near the surface with a factor of 1.7. Generation profiles were obtained from PC-1D for a case with texture on front- and rear side. Screen printed contacts were modelled by assuming that the firing process etches into the diffusion. Diffusion profiles were based upon ECV measurements of the actual doping profiles used in the experiment.

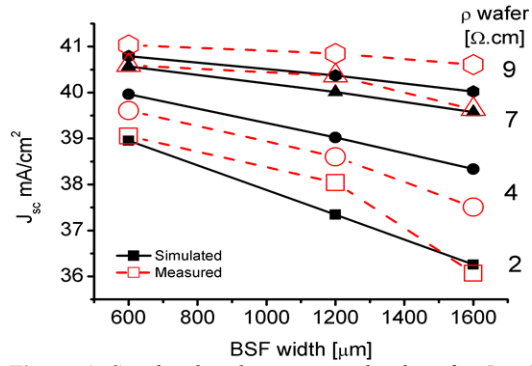


Figure 6: Simulated and experimental values for J_{sc} of the Mercury cells with different wafer resistivity and different BSF full widths. The emitter width is fixed to 1.6 mm.

2.4 Current status of cell performance

Mercury cells of 156x156 were processed on semisquare n-Cz wafers using the same process equipment as our industrial n-Pasha cell process. Screen printed metallization was used and an isolation gap between rear emitter and was omitted mainly for process simplicity. Additionally, 6 inch substrates with multiple small cells were prepared to study the impact of the BSF width. I-V measurement on the small cells was performed by illuminating the active part of the cell between two emitter busbars but including a BSF busbar. We obtained a maximum efficiency of 19.4% with a J_{sc} of 41.6 mA/cm² for a 0.6 mm wide BSF. The high J_{sc} proves that bulk lifetime and front surface passivation are sufficient for near ideal current collection. Very high J_{sc} values up to 41.2 mA/cm² were even reached for cells with an extremely wide BSF of 1.6 mm, demonstrating the effectiveness of the Mercury concept. For the 6 inch cells

we obtained a best cell efficiency of 19.6% (full size illumination) as shown in Table 1. The efficiency loss of the Mercury cells at low bias light conditions compared to 1 sun was analysed. In contrast to earlier reports on linearity issues with IBC cells employing an FFE [11], the efficiency loss at low illumination intensity was not problematic; comparable to a standard p-type reference cell. The IV measurements have been conducted with a Class AAA solar simulator (Wacom). The IV measurements where checked for capacitive effects of the cells: they were performed at ramp rates between 0.1 V/s and 4V/s. The results mentioned in Table 1 are not affected by capacitive effects.

Table 1: Current-voltage parameters of best Mercury IBC cells.

BSF	Emitter	Area	V_{oc}	J_{sc}	FF	eta
mm	mm	cm ²	mV	mA/cm ²	%	%
0.6	1.6	13	627	41.6	74.2	19.4
1.6	1.6	13	629	41.2	73.1	18.9
1.2	1.6	239	635	40.5	73.9	19.0
0.35	0.83	239	642	40.1	76.2	19.6

3 MODULE INTERCONNECTION RESULTS

3.1 Interconnection design optimization

ECN has experience for more than a decade in developing module technology for back-contacted solar cells based on patterned conductive foil [21-23]. In the meantime this technology has been adopted by several commercial parties. In these foil-based modules, the foil takes care of the series-connection of every two adjacent cells and the connection from foil-to-cell is currently realized by tiny dots of Electrically Conductive Adhesive (ECA) that cure simultaneously with EVA during module lamination. In the past, reliability tests on modules manufactured with this technology, but with at the time Metal Wrap Through cells rather than IBC cells, gave excellent results [23]. At ECN we have an integrated approach towards module architecture from which all components, from cells to conductive foil are considered to optimize our modules.

In this work we performed a simulation study in order to optimise the module architecture for maximum efficiency on the one hand and for minimum cost in terms of $\mathsf{C/W_p}$ on the other hand. The parameters that were considered in this optimization study are listed in Table 2. These parameters refer to the cell metallization design of Figure 7, where one can perceive busbars in one direction and fingers in the perpendicular direction. The metal pads that are visible are the contacting areas for the ECA in the module and therefore also dictate the Cu-foil pattern.

The efficiency was computed as follows: First, IV curves were computed, with the software package Atlas (Silvaco), on the basis of 2D unit-cells, consisting of half of an emitter region and half of a BSF region. In the unit-cell computations the pitch has been varied as well as the number of fingers per emitter region (FER) and per BSF region (FBR). These 'bare' IV curves were corrected for the 'external' series resistance, which is covering the Ohmic losses in the fingers, the busbars, the ECA dots and the conductive foil and which was computed analytically. Technically, this series resistance is therefore a function of the nine parameters listed in Table 2. From the 'corrected' IV curve the efficiencies, and

obviously also the maximum one, could be determined, per point in this nine dimensional parameter space.

The costs were composed of fixed cost and variable cost. In this study we considered the amount of ECA and the cell metallization as variable cost components, whereas all other costs (glass, foil, EVA, wafers, processing cost etc.) were simply lumped in one, fixed, number. The ECA cost obviously is proportional to the number of ECA dots per cell (NECA), given by NECA=NBB*NBC+NEB*NEC. The cost of the cell metallization was assumed to be proportional to coverage fraction. The latter is a function of all nine parameters of Table 2 and can be computed in a straight-forward way.

Table 2: Parameters varied in the optimization study

Para- meter	Explanation	Unit
BBW	Base busbar width (at the basis of a tapered busbar)	um
EBW	Emitter busbar width (at the basis of a tapered busbar)	um
NBB	Number of base busbars	
NEB	Number of emitter busbars. NEB=NBB+ i , where i = -1,0,+1	
NBC	Number of base contacts per base busbar.	
NEC	Number of emitter contacts per emitter busbar.	
Pitch	Heart-to-heart distance between two closest emitter regions.	um
FER	Number of fingers per emitter region (1 or 2)	
FBR	Number of fingers per base region (1 or 2)	

For the maximum-efficiency module determination we could observe a maximum that was positioned at quite high metallization fractions, typically 18-20% (screen print properties). It should be noted that for higher metallization fractions the negative impact due to increased contact recombination becomes stronger than the gain in fill-factor. For the minimum €/W_p modules the metallization fraction is tending towards much lower coverage fractions, namely 13-14%. Obviously this can be ascribed to the relatively high contribution to the cost of Ag. For this ε/W_p minimum, typically a series resistance increase of typically 0.5 Ω -cm² (~3%-rel FF decrease) compared to the max- η case has to be accepted. Another trend that can be observed in the parameter space is the tendency towards more contact pads and thus more ECA dots. Although costs are associated with Agcontaining ECA-dots, more dots turn out to beneficial since this enables an Ag-consumption reduction on cell level, because basically the busbars can then become narrower. In our case, however, the number of dots was capped due to a technological constraint we are currently facing in module manufacturing, but it illustrates that if these constraints will be abolished further E/W_p reduction lies ahead. Another important opportunity is to realize narrower metallization lines, which in our case was illustrated by a comparison between screen print and stencil print cases. Here we could observe a cost reduction of even 3 \in cts/ W_p for stencil printing. This can be ascribed to a lower contact recombination (for fixed number of fingers) and thus a higher η , but more importantly due to a cost reduction due to a lower Ag consumption.

Due to the big parameter space mentioned before, we

computed hundred thousands of cases to find the mentioned η -maximum and ε/W_p minimum. Table 3 shows our resulting configuration.

3.2 Current interconnection and cell design

The current interconnection design is summarized by Table 3 and resembles the optimal case within the technological constrains applicable at the moment. The design was optimal for both η -maximum and ℓ/W_n minimum.

Currently two different unit cell dimensions are applied to the interconnection design summarized in Table 3. We employ a unit cell design with relative small pitch comprising of a BSF and emitter width of 0.35 mm and 0.83 mm to showcase the best possible cell conversion efficiency of the Mercury concept with current processing based on screen-printing. The second design consists of a relative wide BSF and emitter of 1.0 mm to illustrated the performance of wide BSF regions. In both cases no gap exists between both polarities and each diffused finger is contacted with one metal finger. The design is illustrated in Figure 6.

Table 3: Current interconnection design both for η-maximum and $€/W_p$ minimum with the technology constraints:

Pads	number
NBB	5
NEB	4
NBC	8
NEC	8
FER	1
FBR	1

Lastly, it is interesting to mention the reverse current properties of these IBC cells which are fabricated without gap between the emitter and BSF. The cells have a low breakdown voltage which results in 9 A current at -3 V. This is an attractive property in case of shading the cells in the module as the maximum power dissipated is only 27 W which prevents heating of the module as also discussed by Bende et al. [25]



Figure 7: Metallization design - BSF and emitter of 1.0 mm full width

3.3 Reliability testing

In order to assess compatibility of Mercury cell with the existing back-contact assembly equipment and module manufacturing conditions, and also evaluate reliability of the resulting PV modules, we have manufactured a series of four-cell IBC modules. These modules were assembled on a semi-automated module assembly pilot line (Eurotron, The Netherlands) using commercially-available materials and then laminated in a three-chamber laminator (3S, Meyer Burger, Switzerland). Therefore, the modules were manufactured under realistic manufacturing conditions, although the bills of materials and process parameters should be optimized in order to minimize the cell-to-module differences (work in progress).

The IBC modules were subjected to thermal cycling (TC) or exposed to damp heat (DH) conditions, as defined in IEC61215. In order to achieve a higher level of acceleration (at least for DH test) we did not frame the modules. As shown in Table 4, all modules showed power output (Pm) loss less than 5% and hence passed both tests. We observed no changes in visual appearance of the modules. Extended climate chamber tests are currently in progress.

Table 4: Relative CTM change for 2×2 IBC modules after TC200 and DH1000 tests.

arer rego and Birroot tests.						
	Relative CTM change [%]*					
Test	Isc	SD	FF	SD	Pm	SD
DH1000	-0.53	0.14	-1.63	0.18	-2.24	0.1
TC200	-0.45	0.47	-0.16	0.05	-0.51	0.5

^{*} Average for three modules.

4 INDUSTRIAL IMPLEMENTATION AND IMPLICATIONS FOR MODULE DESIGN

To realize high efficiencies at low cost, ECN has developed the n-Pasha solar cell concept on n-type Czochralski (Cz) base material [26]. The n-Pasha cell (See Figure 1) is a bifacial solar cell concept based on an n-type wafer. Recently, we have reported n-Pasha cells with an average efficiency of 20%, and top efficiencies of 20.5% on high quality Cz material [27]. All processing steps used for the n-Pasha cell are industry compatible. Our IBC process employs processing steps as in the n-Pasha process, however it includes a patterning step to create the mixed polarity at the rear side of the cell. Due to the synergy with the n-Pasha process, and the relaxed constraints on the cell geometry of the FFE compared to the FSF this will be an industrially feasible process.

A second key technology is ECN's module back-contact technology, which has been originally developed and applied for MWT cells [21-23]. It is based on an integrated conductive back-foil and allows to reduce cell-to-module power loss compared to a conventional tabbing technology, as used to interconnect the n-Pasha cells. Also, the module manufacturing based on integrated back-foil can be done with higher yield and reduced interconnection-process-related stress, allowing use of (much) thinner cells and therefore offering additional cost reduction possibilities. The cell interconnection based on an interconnection foil with integrated copper or aluminium conductor layer can be

optimized for low series resistance losses and significantly reduced efficiency loss from cell to module, since the constraints related to normal front-to-back tabbed interconnection (i.e., shading loss and series resistance from the tab, and stress on the cell) are absent. The mechanical stress induced on the cells by conductive adhesive based interconnection (used in our MWT modules) is low, and as a result, the breakage is reduced. The MWT module technology passes the IEC61215 standard.

This module technology is well suited to use with Mercury IBC cells. Compared to a tab-based interconnection, the rear-side foil interconnection allows to reduce the module series resistance by using more interconnect metal (more cross-sectional area) and thereby reducing the cell-to-module FF loss. In the tabbed case, collected current needs to pass through broad busbars on the cell which can easily measure millimetres in width. In an FSF cell these areas would significantly increase electrical shading losses as calculated by Hermle et al. [10]. In this report an emitter and a BSF busbar of 3 mm on a 125 mm wafer would result in a 0.8% abs efficiency loss. This loss is explained by FF loss above the emitter busbar and electrical shading losses above the BSF busbar. The Mercury cell would significantly mitigate the part of the electrical shading losses as illustrated in the previous sections. The flexibility of the conductive foil interconnection technology allows to increase the number of interconnection points while optimising their distribution on the cell. As a consequence, grid related series resistance can be reduced and busbars can be slimmed down allowing reduction of the metal load on the wafer.

5 CONCLUSIONS

We proposed a novel design variation of a traditional IBC cell, named the Mercury cell, that features a relatively conductive front floating emitter ($<100 \ \Omega/\Box$) and a broad BSF. This configuration significantly alleviates the problem of electrical shading especially at higher wafer resistivity and allows to design efficient IBC cells with interdigitated BSF and emitter regions of equal widths. For the case of equal recombination properties for the FFE and FSF cell, the efficiency potential of the Mercury cell is comparable to FSF IBC with narrow BSF and a case for efficiencies higher than 23% is discussed. Apart from relaxed alignment tolerances for the patterning and metallization steps of the solar cell process, equal widths of both polarities allow to metalize the IBC cell with blanket metallization technologies such as PVD and plating without the need of an isolation layer. This is a significant process simplification and thus an opportunity for cost reduction. We explain the working mechanism of the Mercury cell and present data that validates the model.

So far our best cell efficiencies obtained for this cell concept is 19.6 % on 6 inch cells with a BSF width of 0.35 mm. On 13 cm², we reached 19.4% with a high Jsc value of 41.6 mA/cm² for a front floating emitter cell with an BSF width of 0.6 mm. This high current was nearly maintained at an extremely wide BSF of 1.6 mm, illustrating excellent front passivation for efficient current collection and minimal electrical shading losses. The efficiency of the cells prepared is currently mainly limited by the FF but especially the $V_{\rm oc}$ of the cell.

The number of interconnection designs have been optimized with respect to the cost of electrically conductive adhesive and silver paste load on the wafer and cell performance, expressed in ε/W_p . The design is presented and consists of 62 interconnection pads. The reliability of this design has been tested on 4 cell modules in terms of Thermal cycling and Damp Heat according to the IEC61215 protocol. All tested modules passed the reliability test.

6 APPENDIX:

Table 5: Input parameters for Quokka simulation results presented in Figure 4 and 5:

Diffusion	j0 fA/cm ²	Rsht Ω/sq
BSF	72	65
BSF contact	500	65
Emitter	57	65
emitter contact	450	65
FSF	15	100
FFE	15	100/200
Contact width	25 μm	
nr. BSF contacts	1 or 2	
nr. Emit. contacts	1 or 2	
t_{bulk}	4 ms	
ρ wafer	$6 \Omega.cm$	

6 REFERENCES

- Smith et al. "Towards the Practical Limits of Silicon Solar Cells", Proc. 40th IEEE PVSC, Denver, 2014.
- [2] Fong et al., "Optimisation of n+ diffusion and contact size of IBC solar cells", Proc. 28th EU-PVSEC, Paris (2013)
- [3] B. O'Sullivan et al, "Process simplification for high efficiency, small area interdigitated back contact silicon solar cells", Proc. 28th EU-PVSEC, Paris (2013)
- [4] Bosch SE, press release (2013).
- [5] C.B. Mo et al., Proc. 27th EU-PVSEC, Frankfurt, Germany (2012).
- [6] A. Halm et al. "The Zebra Cell Concept Large Area n-Type Interdigitated Back Contact Solar Cells and One-Cell Modules Fabricated Using Standard Industrial Processing Equipment", 27th EU-PVSEC, Frankfurt, Germany (2012).
- [7] Dong et al., "High-Efficiency Full Back Contacted Cells Using Industrial Processes" Proc. 39th IEEE PVSC, Tampa, (2013)
- [8] I. Cesar at al. "Mercury: A Back Junction Back Contact Cell With Novel Design For High Efficiency And Simplified Processing", Energy Procedia, 4th Int. Conf. on Silicon Photovoltaics, Silicon PV (2014).
- [9] Müller et al., "Back-junction back-contact n-type silicon solar cell with diffused boron emitter locally blocked by implanted phosphorus", Applied Physics Letters, 105, 103503 (2014)
- [10] M. Hermle et al., "Shading Effects in Back-Junction Back-Contacted Silicon Solar Cells", Proc. 33rd IEEE Photovoltaic Specialists Conference, St. Diego, CA, (2008).

- [11] Granek et al, "Analysis of the current linearity at low illumination of high-efficiency back-junction backcontact silicon solar cells", phys. stat. sol. (RRL) 2, No. 4, 151–153 (2008)
- [12] Dicker et al., "Analysis of one-sun monocrystalline rear-contacted silicon solar cells with efficiencies of 22.1%", JAP vol 91,7, (2002)
- [13] P. Basore et al, "All-aluminum Screen-printed IBC Cells: Design Concept", 39th IEEE PVSC, Tampa, 2013
- [14] Robbelijn et al., "Towards advanced back surface fields by boron implantation on p-type interdigitated back junction solar cells", Proc. 5th W-PVSEC, 6-10 September (2010).
- [15] Chan et al.," Simplified interdigitated back contact solar cells", Proc. SiliconPV: April 03-05, 2012, Leuven, Belgium, published in Energy Procedia 27 (2012) 543 – 548.
- [16] Gutiérrez et al., "Industrial manufacturing process of silicon TWT solar cell", Proc. 19th EU-PVSEC, Paris, France (2004).
- [17] Jimeno et al., "Modelling the TWT structure", Proc. 19th EU-PVSEC Paris. France (2004).
- [18] Sah et al., US patent nr 4665277, (1987).
- [19] Sidhu et al., "Interdigitated Back Contact Silicon Solar Cells with Laser Fired Contacts", Proc. 39th IEEE PVSC, Tampa, (2013).
- [20] Granek et al., "Enhanced lateral current transport via the front N+ diffused layer of n-type high-efficiency back-junction back-contact silicon solar cells", Prog. Photovolt: Res. Appl. V17,1 p47-56, (2009).
- [21] M.W.P.E. Lamers et al., "17.9% back-contacted mc-Si cells resulting in module efficiency of 17.0%", Proc. 25th EU-PVSEC, (2010), p.1417.
- [22] N. Guillevin et Al. "High efficiency n-type Metal-Wrap-Through cells and modules using industrial processes", SNEC conference Shanghai, (2014).
- [23] I. Bennett et al, "Reducing the Cost of Back-contact Module Technology", Energy Procedia Proceedings of the 3rd International Conference on Crystalline Silicon Photovoltaics (SiliconPV 2013) volume 38, (2013), Pages 329–333
- [24] A. Fell, "A free and fast three-dimensional/two-dimensional solar cell simulator featuring conductive boundary and quasi-neutrality approximations," IEEE Trans. Electron Devices, vol. 60, no. 2, pp. 733–738, Feb. (2013).
- [25] E.E. Bende et al., "Performance and safety aspects of PV modules under partial shading, a simulation study" Proc. 29th EU-PVSEC (2014), Amsterdam, The Netherlands
- [26] I.G. Romijn et al, "Industrial cost effective n-Pasha solar cells with >20% efficiency", Proc. 28th EU-PVSEC (2013), Paris, France
- [27] I.G. Romijn. "Front side improvements for n-Pasha solar cells", SNEC conference, Shanghai, (2014).